https://doi.org/10.5194/egusphere-2026-1290
Preprint. Discussion started: 22 June 2026

Design and evaluation of a specific differential phase estimation algorithm for dual-polarization radar using scale-adaptive local polynomial fitting

Nobuhiro Nagumo[1,2] and Hiroshi Yamauchi[2]

[1]Atmosphere and Ocean Department, Japan Meteorological Agency, Tokyo, Japan
[2] Meteorological Research Institute, Japan Meteorological Agency, Tsukuba, Japan

Correspondence to: Nobuhiro Nagumo (nagumo@met.kishou.go.jp)

Abstract. We propose a method for estimating the specific differential phase (K_{DP}) with high spatial resolution from the received differential phase (Ψ_{DP}) observed by dual-polarization radar and then evaluate the performance of the estimated K_{DP}. Because Ψ_{DP} contains noise, its range derivative, K_{DP}, is prone to significant errors. The proposed method performs scale-adaptive local polynomial fitting, wherein the fitting window is dynamically adjusted based on the magnitude of the K_{DP}. This adjustment enables high resolution in regions with large K_{DP} and noise suppression in regions with small K_{DP} through optimal setting of parameters. The method was applied to Ψ_{DP} data from both idealized synthetic experiments and actual radar observations. Compared to existing algorithms, the method improved noise suppression in low-K_{DP} regions while enhancing accuracy in regions exhibiting fine-scale K_{DP} variation. The good agreement of the results with Ψ_{DP} in terms of the cumulative phase shift demonstrated a balance between fine-scale accuracy and robustness.

1 Introduction

Dual-polarization radar differs from single-polarization radar systems in that its transmission and reception of horizontally and vertically polarized waves enables the derivation of multiple physical parameters. These parameters contribute to better quality control and more accurate estimation of precipitation intensity, as well as enabling the use of particle classification algorithms that were not possible with single-polarization radar (Bringi and Chandrasekar, 2001; Ryzhkov and Zrnić, 2019). Among these parameters, the specific differential phase (K_{DP}) represents the azimuthal variation per unit distance of the phase difference between horizontally and vertically polarized waves transmitted by radar. Since K_{DP} is unaffected by attenuation, unlike reflectivity, and is relatively insensitive to variations in the drop size distribution, it has been recognized as a promising parameter for improving the accuracy of rainfall estimates (e.g., Brandes *et al.* 2002). K_{DP} is defined as the range derivative of the differential phase (Φ_{DP}), which represents the accumulated phase difference between polarizations along the radar propagation path, as defined in Eq. (1):

$$K_{DP} = \frac{1}{2}\frac{d\Phi_{DP}(r)}{dr}\,, \tag{1}$$

where r denotes the range and d/dr represents the derivative with respect to r. However, in dual-polarization radar observations, the measured differential phase Ψ_{DP} includes not only Φ_{DP} but also additional components such as white noise (ϵ) and differential phase shifts caused by non-uniform propagation effects (δ), as expressed in Eq. (2):

$$\Psi_{DP} = \Phi_{DP} + \epsilon + \delta \, . \tag{2}$$

Several approaches for estimating K_{DP} have been proposed to mitigate these influences. Hubbert and Bringi (1995) proposed a technique based on a fixed weighted moving average. Maesaka *et al.* (2012) introduced a variational approach, while Giangrande *et al.* (2013) applied linear programming. The goal in both cases was to retrieve the optimal Φ_{DP} under specific constraints. Local regression techniques that simultaneously perform smoothing and differentiation have also been explored. These techniques have included fitting methods such as the linear least-squares approach applied by Gorgucci *et al.* (1999) and spline-based fitting methods (Wang and Chandrasekar, 2009). Differences of regression definitions give rise to distinct characteristics in the resulting distributions: linear least-squares tends to capture sharp variations more effectively when fewer samples are used for fitting, but this characteristic also increases susceptibility to error, while spline-based fitting methods better preserve continuity between grid points and enable smoother transitions. In recent years, a variety of methods to estimate K_{DP} have been implemented in open-source, radar-processing frameworks. These methods have included Py-ART (Helms and Collis, 2016) and ωradlib (Heistermann *et al.*, 2013) (e.g., Maesaka *et al.*, 2012; Vulpiani *et al.*, 2012; Giangrande *et al.*, 2013; Schneebeli *et al.*, 2014). These methods have also been evaluated by multiple researchers (e.g., Reimel and Kumjian, 2021; Aldana *et al.*, 2025). According to these evaluations, no single method consistently outperforms others; rather, each can achieve improved accuracy when appropriate parameters are selected for the intended application.

Recent developments of K_{DP} algorithms and related techniques have contributed to increasingly refined operational setups for quantitative precipitation estimation (QPE). The precipitation nowcasting system operated by the Japan Meteorological Agency (JMA), for example, achieves a spatial resolution as low as 250 m. As such resolution becomes standard, high-resolution K_{DP} estimates are required to be comparable to it. To incorporate K_{DP}-based estimation while maintaining the resolution of conventional QPE based on the reflectivity factor, it is desirable to apply local regression with narrow computational scales (e.g., Gorgucci *et al.*, 1999), sensitive to resolution and capable of capturing localized variation without excessive smoothing. In contrast, the adaptive control of the fitting range proposed by Wang and Chandrasekar (2009) provides a flexible strategy for appropriately suppressing noise, although its spline-based formulation naturally involves a somewhat broader effective scale. The Savitzky–Golay (SG: Savitzky and Golay, 1964) framework, which can capture localized variations with fewer grid points, is well suited to this purpose.

This paper is organized as follows. Section 2 outlines the basic concept of the developed algorithm and the overall parameter settings. Section 3 describes the specifications of the radar used for evaluation and the associated methodology. Section 4 presents the results and discussion, including parameter tuning under idealized experimental settings, sensitivity experiments using observational data, and comparative analyses with existing products to clarify structural differences and advantages. Section 5 summarizes the study. The Appendices present supplementary functions of the developed algorithm.

2 Fundamental concept of the algorithm

2.1 SG fitting with varying calculation range

In the case of regularly gridded data such as radar observations, SG polynomial fitting serves as a core technique in the present approach for extracting features from noisy input. When estimating the derivative quantity K_{DP} from Φ_{DP}, assuming a second-order polynomial leads to the formulation shown in Eq. (3):

$$K_{\mathrm{DP}}(j) = \frac{\sum_{k=-m}^{m}(k\Phi_{\mathrm{DP}}(j+k))}{\sum_{k=-m}^{m}(k^2)}\,, \tag{3}$$

where j denotes the grid point of interest, and k represents the relative offset from j. This formulation is both simpler and faster than solving the least-squares problem directly. The summation is taken over a symmetric window of width $2m+1$, i.e., k ranges from $-m$ to m. Notably, the coefficient of the linear term in the second-order SG polynomial is mathematically equivalent to the slope obtained by linear regression, and that coefficient thus corresponds to the formulation used by Gorgucci *et al*. (1999). In this study, the range of the calculation used in SG fitting was dynamically adjusted to improve the quality of K_{DP} estimation. When the K_{DP} was large, a narrow range was applied to preserve high resolution; conversely, when the K_{DP} was small, a wider range was used to suppress random noise. Rather than fixing the calculation range m in Eq. (3), the method sequentially varied m to obtain an estimate of K_{DP} that satisfied the desired balance between resolution and stability. To determine when to terminate the adjustment, a threshold was defined for the calculation window based on the phase difference $\Delta\Phi_{DP}$. The algorithm then searched until both m and the resulting K_{DP} asymptotically approached this threshold; this process is formulated in Eq. (4):

$$\Delta\Phi_{\mathrm{DP}} = 2mK_{\mathrm{DP}}(j)\Delta r\,, \tag{4}$$

where, Δr denotes the resolution of the range of the radar bin. Figure 1 illustrates the basic sequential flow of the calculation. In this process, the window parameter m for the SG fitting is adaptively incremented or decremented to find the optimal scale by comparing the value from Eq. (4) with the threshold $\Delta\Phi_{DP}$. The specific definition and criteria for $\Delta\Phi_{DP}$ are detailed as Eq. (5) in the subsequent section.

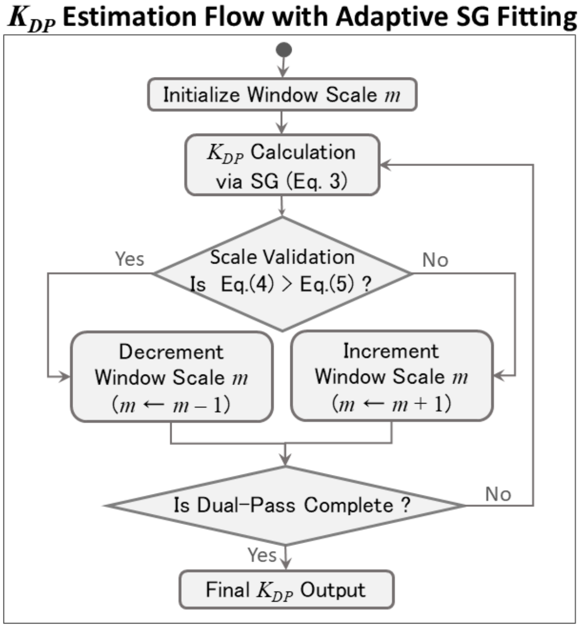

Figure 1: Flowchart for adaptive estimation of K_{DP} using SG fitting.

2.2 Adaptive windowing in SG fitting

The dynamic adjustment of the range of the calculation is subject to two fundamental limitations: it cannot operate below the scale of the grid spacing, nor can it extend to an infinite scale. In Eq. (3), the minimum range of the calculation corresponds to $m = 1$, in which case SG is fit over three grid points. The maximum K_{DP} (K_{DP}^{max}) theoretically computable within this minimal window must be predefined and used as the target value in Eq. (4). In typical precipitation events, K_{DP} values generally lie below 5° km^{-1}. However, in extreme cases such as supercells, excessively large values may occasionally occur because of the presence of wet hail (e.g., Romine *et al.*, 2008; Ryzhkov *et al.*, 2013). Although even higher values are theoretically possible during intense rainfall, this study assumes 20° km^{-1} as a practical upper bound for K_{DP}. Nevertheless, because of contamination of Ψ_{DP} by noise, the exceedance of this threshold by estimated values may prevent satisfaction of the termination condition. To address this possibility, the initial calculation sets the window size using Eq. (5), scaled by a factor a, which will be determined in a later discussion. Furthermore, because negative K_{DP} values may arise in C-band radar observations, a minimum K_{DP} (K_{DP}^{min}) is accordingly defined in Appendix A1.

The window size is given by

$$\Delta\Phi_{DP} = 2aK_{DP}^{max}\Delta r \ . \qquad (5)$$

Another limitation is the inability to design an infinite-scale calculation window. Theoretically, when the window size is fixed and K_{DP} asymptotically approaches zero, the required range m must tend toward infinity to satisfy the window condition. To avoid this impracticality during the sequential estimation process, a small perturbation is introduced by incrementally updating $\Delta\Phi_{DP}$ by ±C at each iteration. The positive and negative signs are applied respectively when the estimated K_{DP} exceeds or falls below the target window defined in Eq. (4). This perturbation is further scaled by an arbitrary coefficient b, and the constant C is then calculated using Eq. (6):

$$C = cns/(ab)\,. \tag{6}$$

Here, placing the coefficients a and b in the denominator intuitively reflects that larger values of these coefficients result in a wider computational window m. The parameter cns is an arbitrary constant and was set to 1 in this study for clarity. Figure 2 illustrates the K_{DP}–m relationship, which encompasses both a design that considers Eqs. (5) and (6) and one that does not. The coefficient a in Eq. (5) simply scales the entire computational window and thus controls the overall smoothness of the precipitation field. In contrast, Eq. (6), which includes b, adjusts the window dynamically: the more sequential computations are performed (i.e., the smaller the K_{DP}), the more the window changes. This mechanism enables a balance between high-resolution representation in regions of intense rainfall and noise suppression through smoothing in areas of light rainfall. It encapsulates radar-specific tuning factors such as radar bin size and radar quality (e.g., Ψ_{DP}-texture).

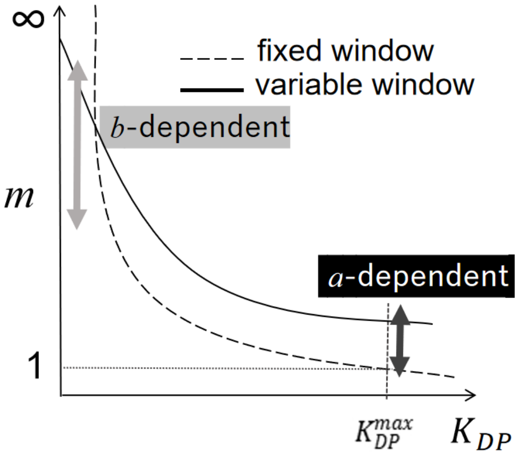

Figure 2: Schematic representation of the K_{DP}–m relationship. The dashed line corresponds to a fixed-window design with the highest resolution, while the solid line reflects a coefficient-adjusted design with controlled resolution. In this adaptive design, K_{DP}^{max}, which is an adjustable parameter based on the maximum K_{DP} expected in nature, is set as the threshold to achieve the highest resolution ($m = 1$).

2.3 Two-stage adaptive SG fitting incorporating δ removal

The SG fitting step suppresses fine-scale random noise (ϵ). In the proposed algorithm, this step is followed by an explicit procedure that reflects the framework of Hubbert and Bringi (1995) and is implemented independently to remove the δ associated with backscattering. To adjust the balance between resolution and noise reduction, the noise threshold varies with K_{DP}: higher values prioritize resolution and lower values prioritize smoothing. This adjustment is expressed as follow:

$$\begin{cases} \Psi_{DP}(j)_{crit} > \Phi_{DP}(j-1) + 2dr\frac{K_{DP}(j-1)+K_{DP}(j)}{2}(1+N_{crit}) \\ \Psi_{DP}(j)_{crit} < \Phi_{DP}(j-1) + 2dr\frac{K_{DP}(j-1)+K_{DP}(j)}{2}(1-N_{crit}) \end{cases}. \tag{7}$$

Equation (7) defines the noise-detection criterion for the observed Ψ_{DP} data. When the initial SG fitting yields Φ_{DP} and K_{DP} values that exceed a certain threshold, Ψ_{DP}. is replaced with Φ_{DP}., which is equated to $\Phi_{DP}(j)$ calculated using Eq. (8). This replacement is controlled by the parameter N_{crit}. If N_{crit} is set to zero, all Ψ_{DP}. values are treated as noise and replaced. If N_{crit} is set to a large value such that no threshold is exceeded, Ψ_{DP}. remains unchanged. By choosing an appropriate intermediate N_{crit} and applying a second SG fitting, K_{DP} can be computed from the δ suppressed data.

The updated Φ_{DP} (j) is then obtained from

$$\Phi_{DP}(j) = \Phi_{DP}(j-1) + 2dr\frac{K_{DP}(j-1)+K_{DP}(j)}{2}. \tag{8}$$

Because our sensitivity tests showed that δ noise suppression behaved reasonably only when the threshold parameter N_{crit} was set between 1 and 3—values below this range filter out almost all gates as noise, while values above it fail to filter extreme noise effectively—we set N_{crit} to 2.0. This stable baseline enabled the second SG fitting to use a narrow window (a = 1) and thereby achieve high spatial resolution while maintaining low noise levels.

3 Configuration and evaluation

3.1 Radar specifications

Radar data provided by the JMA from the Tokyo radar were used in the development and evaluation of the proposed methodology. They were obtained from a solid-state, dual-polarization C-band radar operating at 5.3 GHz, with a beamwidth of 1.1 degrees, an azimuthal resolution of 250 m, and a maximum observation range of 400 km. Excluding vertical scans, the representative elevation angles were 0.0, 0.3, 0.7, 1.1, 1.7, 2.5, 3.5, 4.8, 6.7, 9.3, 12.8, 17.8, and 25.0 degrees. These angles were routinely scanned at 5-minute intervals.

3.2 Algorithm evaluation

The idealized experimental framework described by Reimel and Kumjian (2021) was used to evaluate the proposed algorithm and determine its parameters. This common framework facilitates consistent parameter tuning and enables quantitative comparison of algorithmic characteristics, including the ability to suppress noise. Their first method involves prescribing a Gaussian-shaped K_{DP} field as the ground truth (see Eq. [1] in Reimel and Kumjian [2021]), adding intrinsic random noise to generate synthetic Ψ_{DP} data, and applying the algorithm to estimate K_{DP} to assess deviations from the true field (see Fig. 1 in Reimel and Kumjian [2021] for reference). One of their evaluation metrics is the root mean square error (RMSE) with respect to the true K_{DP}. The parameters of the proposed algorithm were selected to minimize the RMSE. The Gaussian-shaped K_{DP} field used in our evaluation follows the same formulation and is given by Eq. (9):

https://doi.org/10.5194/egusphere-2026-1290
Preprint. Discussion started: 22 June 2026

$$K_{\mathrm{DP}}(r) = K_{\mathrm{DP}}^{max}\exp\left[\frac{-(r-r_0)^2}{2\zeta^2}\right]. \tag{9}$$

In this experiment, the computational domain was set to 50 km, with r_0 centred at 25 km, and the azimuthal resolution was fixed at 250 m. The parameter ζ, representing the width of the Gaussian distribution, ranged from 1 to 10, while K_{DP}^{max}, the peak amplitude of the Gaussian, ranged from 0.5 to 5.0. To obtain reliable RMSE statistics, the experiment was repeated 100 times for each parameter setting. This experiment is referred to as RKF1 in this study.

The second experiment, referred to as RKF6, introduced higher-frequency perturbations following the design in Fig. 6 of Reimel and Kumjian (2021). The noise was configured with a standard deviation of 2.6° to be consistent with prior studies (Liu *et al.*, 1994; Ryzhkov and Zrnić, 1995; Gorgucci *et al.*, 1999; Brandes *et al.*, 2002). This value closely matched the typical phase deviation of about 2.5° observed for the Tokyo radar under stratiform rainfall conditions, based on checks at several arbitrary locations under similar conditions (reflectivity > −10 dBZ, $\rho_{HV} > 0.98$, and a near-surface 3 × 3 km² area). These similarities ensured that the synthetic Ψ_{DP} used in RKF6 was statistically equivalent to the observed differential phase. The evaluation targeted only the initial form of the SG processing described in Section 2.2 and excluded the δ removal and subsequent SG processing discussed in Section 2.3.

4 Results and Discussion

4.1 Relationship between magnitude and resolution of K_{DP}

Figure 3a shows the mean distribution obtained by varying the coefficient *a* while keeping *b* fixed. When *a* was excessively small, the *m*-dependent computation window narrowed, and differences of resolution associated with variations of K_{DP} within typical rainfall intensity ranges become barely distinguishable. Conversely, excessively large *a* values led to an overly broad computation window that resulted in excessive smoothing that could obscure meteorological signals during weak rainfall. The observed tendencies were similar in the reversed case, with *a* fixed and *b* varied (Fig. 3b). In both cases, the results confirmed that appropriate coefficient selection enabled adaptive control of resolution and smoothing in accord with the magnitude of K_{DP}.

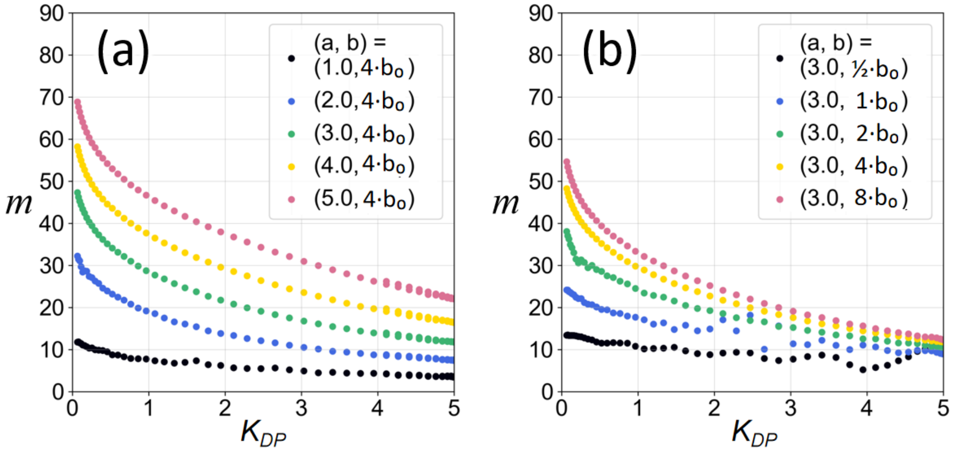

Figure 3: Examples of K_{DP}–m relationship calculations: (a) a varied, b fixed; (b) a fixed, b varied. Each curve represents the mean of 100 experimental trials conducted under RKF1 conditions with $\zeta = 4$ and $K_{DP}^{max} = 10$. A nominal reference value of $b_0 = 3.75$ is used for scaling.

4.2 Parameter setting via idealized experiments

Parameters for the proposed algorithm were optimized using the idealized experimental frameworks of RKF1 and RKF6. Figure 4 presents a representative example from RKF1: the ensemble results of 100 trials, including the mean and standard deviation for each configuration of parameters a and b. The fact that all configurations exhibited unimodal mean distributions cantered around the true signal reflected the zero-phase delay characteristics of the SG method. In all cases, the deviation tended to be smaller for lower K_{DP} values. This smoothing behavior is precisely what sets the proposed method apart from the K_{DP} algorithms introduced by Reimel and Kumjian (2021). Differences of the parameters a and b led to variations of both the mean and standard deviation, depending on the shape of the imposed Gaussian distribution. A narrow distribution with $\zeta = 1$ corresponds to about 10 km in scale, typical of an isolated convective cell. In this case, the use of smaller coefficients yielded higher resolution and mean distributions closer to the true distribution, while larger coefficients produced smoother distributions that averaged out the signal (see Figs. 3a, 3b, 3e, and 3f). A broader Gaussian with $\zeta = 10$ corresponded to about 50 km in scale, which is representative of a multicell convective system. Under this condition, the mean distribution remained close to the true value, regardless of the magnitude of the coefficient. Across all configurations, the deviation increased with the magnitude of K_{DP}. The standard deviation became smaller when coefficients a and b were larger because the smoothing effects were stronger (see Figs. 3c, 3d, 3g, 3h).

In this experiment, ζ represented the scale of the phenomenon, and coefficients a and b functioned as adjustable filter strengths for perturbations at each scale. While noise suppression was essential, excessive filtering could remove fine-scale perturbation components that were close to noise. Therefore, a and b were determined through a comprehensive minimization of the overall RMSE across various scales of phenomena in the RKF1 experiments.

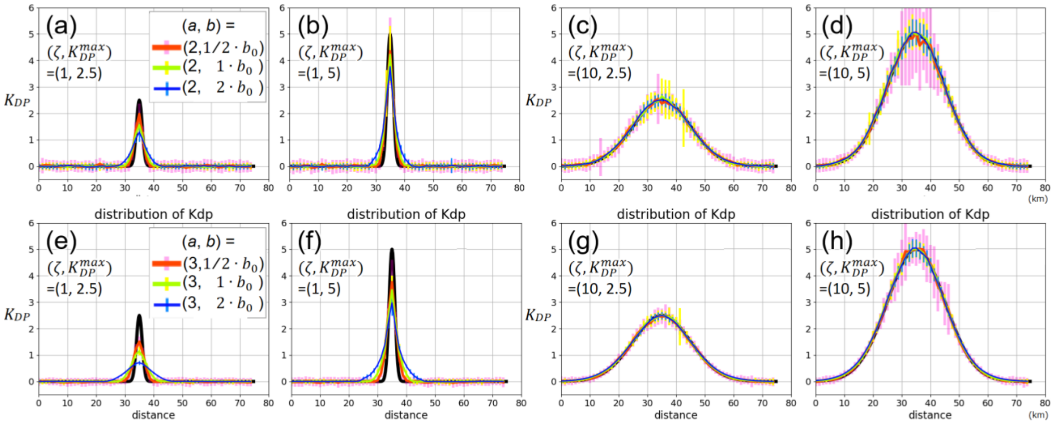

Figure 4: Results from RKF1 experiments repeated 100 times. Black is the true profile used as input in all runs. Each panel shows the mean and standard deviation of the estimated K$_{DP}$ based on inputs randomly perturbed from the true profile, with combinations of ζ = 1, 10 and K_{DP}^{max} = 2.5, 5. The estimation model includes two coefficients, *a* and *b*, which were varied to assess sensitivity: *a* was fixed at either 2 or 3 (upper and lower rows, respectively), while *b* varied across ½ *b*₀, 1 *b*₀, and 2 *b*₀ (red, green, and blue, respectively). Other combinations of ζ and K_{DP}^{max} were tested but have been omitted here for brevity. The nominal reference *b*₀ was the same as in Fig. 3.

Figure 5 presents a heatmap of RMSE values computed across multiple combinations of the smoothing parameters *a* and *b*. Smaller values of *a* and *b* corresponded to narrower computational windows that resulted in insufficient smoothing and elevated RMSEs. In contrast, larger values led to broader averaging, which reduced the fidelity of narrow-band structures (e.g., Gaussian profiles with ζ < 2). Because excessive RMSEs should be avoided, moderate values of the parameters *a* and *b* are desirable to achieve appropriate smoothing without over- or under-filtering. In the RKF1 experiment, comprehensive evaluation revealed a region of relatively low RMSE near the centre of the figure, corresponding to approximately *a* = 2–2.5 and *b* = (1–2) b_0, with b_0 = 3.75.

Figure 6 focuses on the central region of Fig. 5 and presents a heatmap of the maximum RMSE values for each combination of *a* and *b*, extracted from all RKF1 experiment configurations—that is, across all combinations of ζ and K_{DP}^{max}. This figure demonstrates that, within the examined range, there exists an appropriate setting of *b* for each *a* that effectively suppresses the maximum RMSE.

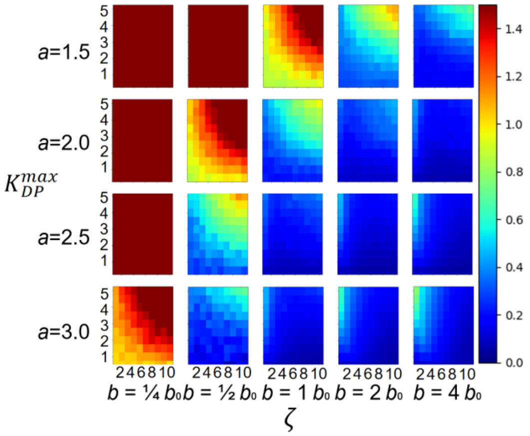

Figure 5: RMSE heatmaps from RKF1 experiments under various combinations of the coefficients *a* and *b*. Each panel shows RMSE values over a 10×10 grid, with ζ ranging from 1 to 10 on the x-axis and K_{DP}^{max} from 0.5 to 5.0 on the y-axis. The nominal reference *b*₀ is the same as in Fig. 3.

225

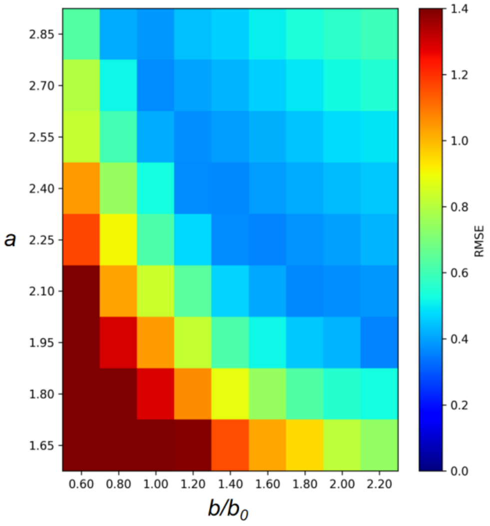

Figure 6: Heatmap of the maximum RMSE across ζ settings for each combination of coefficients *a* and *b* in the RKF1 experiments. For each (*a*, *b*) pair, the highest RMSE observed across all ζ values is plotted. The vertical axis represents *a*, and the horizontal axis represents *b* normalized by *b*₀ as in Fig. 3.

The RKF6 experiment was designed to evaluate the impact of precipitation fields characterized by diverse perturbations. It therefore extended the precipitation fields beyond the idealized Gaussian profile used in RKF1. Figure 7 shows the results of 100 repeated trials for various combinations of smoothing parameters a and b, including the true KDP profile (red), the individual estimates (grey), and their mean (black). When *a* and *b* are small (i.e., the computational window is narrow), high-frequency fluctuations, including both noise and fine-scale signals, are retained. This retention helps preserve mean values close to the ground truth, but it also leads to high variability. Conversely, when *a* and *b* are large (i.e., the window is wide), true fine-scale signals are also smoothed out. The result is lower variability but biased mean estimates. For low-resolution products, broader smoothing is generally acceptable because the loss of fine-scale signals has a negligible impact, and noise can be effectively suppressed. In contrast, high-resolution retrievals tend to retain residual noise, which may reduce the reliability of the estimates if used directly. However, the preservation of the underlying mean structure suggests that high-resolution outputs are not necessarily unsuitable for QPE. Rather, when the objective is to represent spatially averaged quantities at specific scales, the noise inherent in high-resolution estimates becomes less critical. In fact, such averaged outputs can yield more representative results than low-resolution alternatives, which may have already lost essential structural information through excessive smoothing. The optimal trade-off between noise and resolution is broadly consistent with the findings of the RKF1 experiment.

It should be noted that the noise field used by Reimel and Kumjian (2021) was randomly generated and independent of K_{DP}. In reality, white noise depends on the signal-to-noise ratio and tends to be less prominent in high-K_{DP} regions. Their experiment may not fully reflect the actual noise in intense precipitation areas, and the actual level of noise might be lower than what is shown in Fig. 7. This characteristic should also be evaluated for realism using actual observational data. In the following sections, we present the results of case studies using the specific parameters $a = 2$ and $b = 2b_0$.

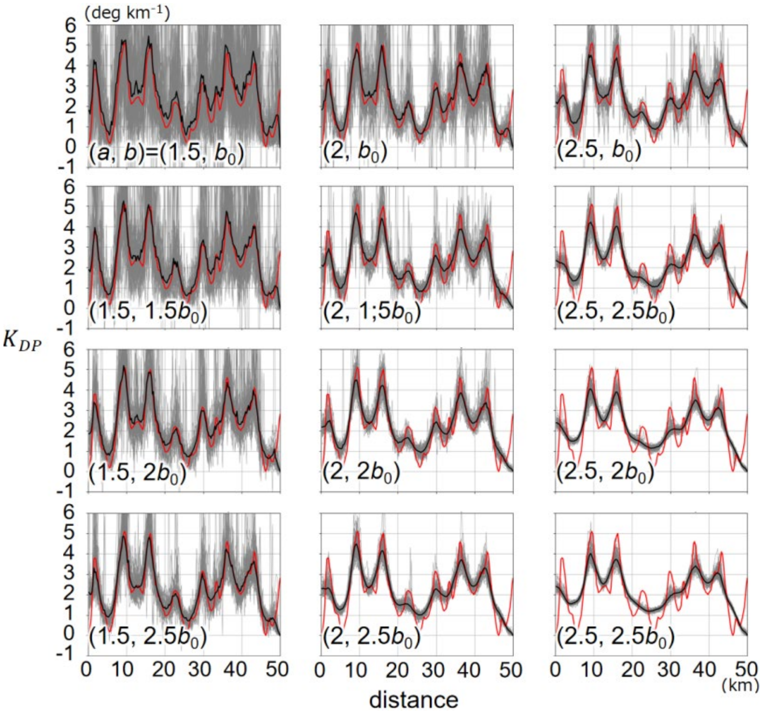

Figure 7: Values of the specific differential phase (K_{DP}) from RKF6 experiments repeated 100 times for each coefficient *a* and *b*, using the same setup as in RKF1 (Fig. 4). The red line shows the true K_{DP} profile, grey lines the individual estimates, and the black line their mean. The reference value b_0 is the same as in Fig. 3.

4.3 Evaluation of K_{DP} estimation using radar observations

Figure 8a shows the attenuation-corrected reflectivity (Z; Jamesen, 1992; Bringi and Chandrasekar, 2001) from the Tokyo radar at 0.7° elevation, observed at 0145 UTC on 27 May 2022. The echo exhibits a narrow north–south convective rainband moving eastward toward the radar centre. The rainband structure features embedded precipitation cells aligned along its length. Figure 8b shows Z from the same radar at 0345 UTC on 16 January 2023, during a winter event with surface temperatures around 6 °C. At an elevation of 0.7°, the bright band is evident as a broad enhancement of Z within the range of 50–100 km from the radar. This structure indicates melting processes and the presence of ice crystals aloft.

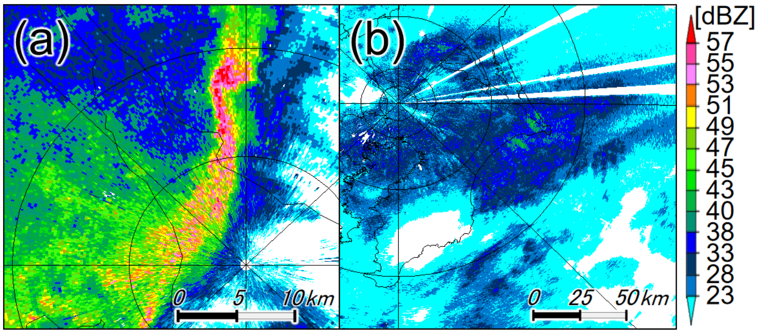

Figure 8: Attenuation-corrected reflectivity distributions for two individual cases: (a) 0114 UTC on 27 May 2022, rainy season convective echo (elevation angle 1.7°); (b) 0345 UTC on 16 January 2023, winter case with wet snow and snow aloft (surface temperature ~6 °C; elevation angle 0.7°).

Figure 9 compares the K_{DP} distributions and Z–K_{DP} relationships for the two observational cases using the method of Hubbert and Bringi (1995) (hereafter *HB*; see Section 4.2 for parameter settings) and a newly developed version (hereafter *Dev*). Note that for each method, the reflectivity factor (Z) was independently corrected for attenuation using its respective K_{DP} field. In *HB*, convective regions with high rates of rainfall appear unnaturally elongated in the azimuthal direction. In addition, pronounced variability—including large positive and negative perturbations—is also stretched and amplified in regions of weak rainfall and layers of melting ice (Figs 9a, 9e). As a result, there are large perturbations (1–2 ° km^{-1}) in the statistical Z–K_{DP} relationship, even at low values of the reflectivity ($Z < 20$ dBZ), and the peak correlation between Z and K_{DP} appears misaligned (Figs. 9c, 9g). In contrast, *Dev* suppresses variability in regions of weak rainfall (Fig. 9d) and also mitigates the pronounced fluctuations associated with layers of melting ice (Fig. 9h). At the same time, *Dev* successfully reproduced narrow convective echoes (1–2 km wide) without excessive smoothing (Fig. 9b). Within the rainband structure, several high values of K_{DP} were also embedded in cell-like formations. Statistically, *Dev* yielded a smooth exponential relationship between Z and K_{DP} across regimes of both weak and strong rainfall (Fig. 9d). This behavior closely aligned with the results of Wang and Chandrasekar (2009) and represented the expected performance for methods that utilize a dynamic computational window.

https://doi.org/10.5194/egusphere-2026-1290
Preprint. Discussion started: 22 June 2026

Figure 10 shows an enlarged view of the region of intense rainfall in Fig. 9b and displays the Z and K_{DP} fields across multiple elevation angles. For example, the fact that areas with strong reflectivity (>55 dBZ) are also characterized by high K_{DP} values is indicative of vertically consistent, intense rainfall. In regions with weaker precipitation, K_{DP} fields appear smoother and show less contrast compared to Z.

Figure 11 overlays the K_{DP}- and Z-based rainfall profiles along the A–B line shown in Figs. 10b and 10f. These profiles exhibit similar variations of intensity derived from both K_{DP} and Z. The implication is that K_{DP}-based estimates retain spatial resolution comparable to Z in regions of intense precipitation. This result is consistent with the strong correlation between Z and K_{DP} observed in Fig. 9d, even at the local scale. However, in areas where reflectivity exceeded 55 dBZ, localized K_{DP} enhancements were apparent. These features suggested the potential influence of contamination by hail (e.g., wet hail), consistent with previous findings (Romine et al., 2008; Wilson and Van Den Broeke, 2021).

It should be noted that for the case studies, the *Dev* method incorporates extrapolation near the radar centre to ensure domain coverage and interpolation over echo-free regions (Appendix B). These processes, along with explicit quality control of noise (Appendix C) and a sequential termination algorithm designed for operational efficiency (Appendix D) were implemented to facilitate practical application without materially affecting the core results.

https://doi.org/10.5194/egusphere-2026-1290
Preprint. Discussion started: 22 June 2026

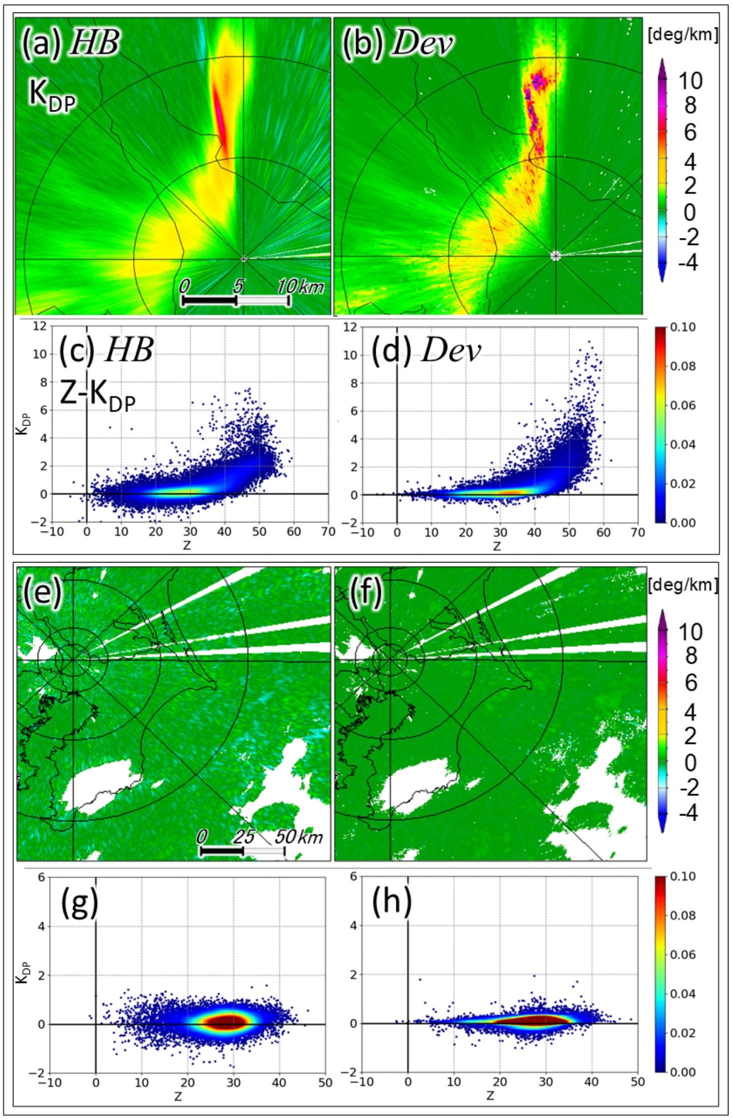

Figure 9: Two-dimensional distributions of K_{DP}(*HB*) derived from Hubbert and Bringi (1995) and the developed K_{DP}(*Dev*) shown alongside Z–K_{DP} scatterplots. Panels (a–d) correspond to Fig. 8a, and panels (e–h) to Fig. 8b.

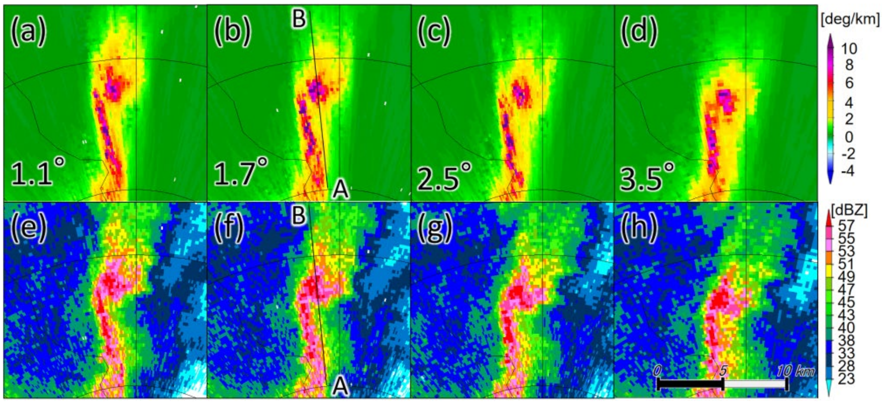

Figure 10: Enlarged views of K_{DP} and Z from the same *Dev* case as in Fig. 9b, shown at elevation angles of 1.1°, 1.7°, 2.5°, and 3.5°.

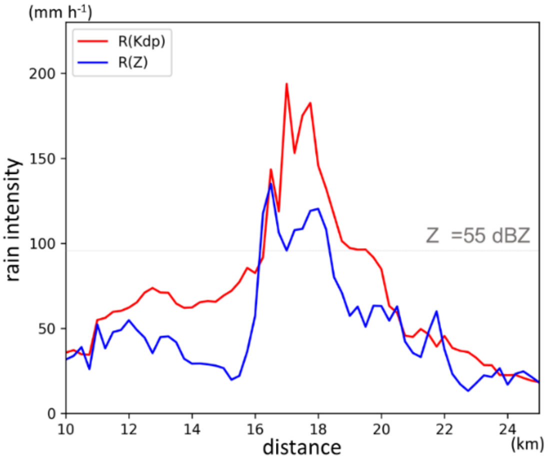

Figure 11: Distributions of K_{DP} and Z along the A–B line from the *Dev* case shown in Figs. 9b and 9f, converted to rainfall rate using the relations $Z = 200R(Z)^{1.6}$ and $R(K_{DP}) = 129(K_{DP}/f)^{0.85}$ (e.g., Marshall and Palmer 1948; Bringi and Chandrasekar 2001). Radar frequency f is given in MHz. Dashed line indicates the reference R(Z) line for 55 dBZ.

4.4 Comparison of algorithms for reproducing K_{DP} from radar data

Figure 12 compares the *Dev* method with three existing algorithms (Hubbert and Bringi, 1995; Maesaka *et al*., 2012; Giangrande *et al*., 2013) along the A–B transect shown in Fig. 10b. Compared to *Dev*, the *HB* method yielded noticeably smoothed K_{DP} estimates (Fig. 12a), and the deviation of the corresponding integrated Φ_{DP} distribution from the reference Ψ_{DP} suggested that repeated moving averages suppressed fine-scale precipitation structures and local intensity gradients (Fig. 12d). The algorithm of Maesaka *et al*. (2012) better preserved peak features relative to *HB* (Fig. 12b), and its Φ_{DP} distribution was closer to Ψ_{DP}; however, because its parameter settings are fixed, it failed to capture sub-10 km perturbations (Fig. 12e). The algorithm of Giangrande *et al*. (2013) produced K_{DP} distributions that varied with the choice of parameters (Fig. 12c), but the Φ_{DP} derived via linear programming (LP) closely resembled that of *Dev* (Fig. 12f). Notably, the K_{DP}

output with a higher-resolution setting of the window length (w_len = 5) captured peak signals similar to the observations and *Dev*. However, it exhibited a different trade-off: it gave less emphasis to the consistency of fluctuations across both intense and weak precipitation than the *Dev* method.

The *Dev* method provides higher resolution of intense rainfall and a more effective trade-off against weak-rain noise compared to other algorithms. While the integrated Φ_{DP} is generally reliable, its ability to represent resolution at the boundaries of intense and light rain requires further refinement, which will be the focus of our next report.

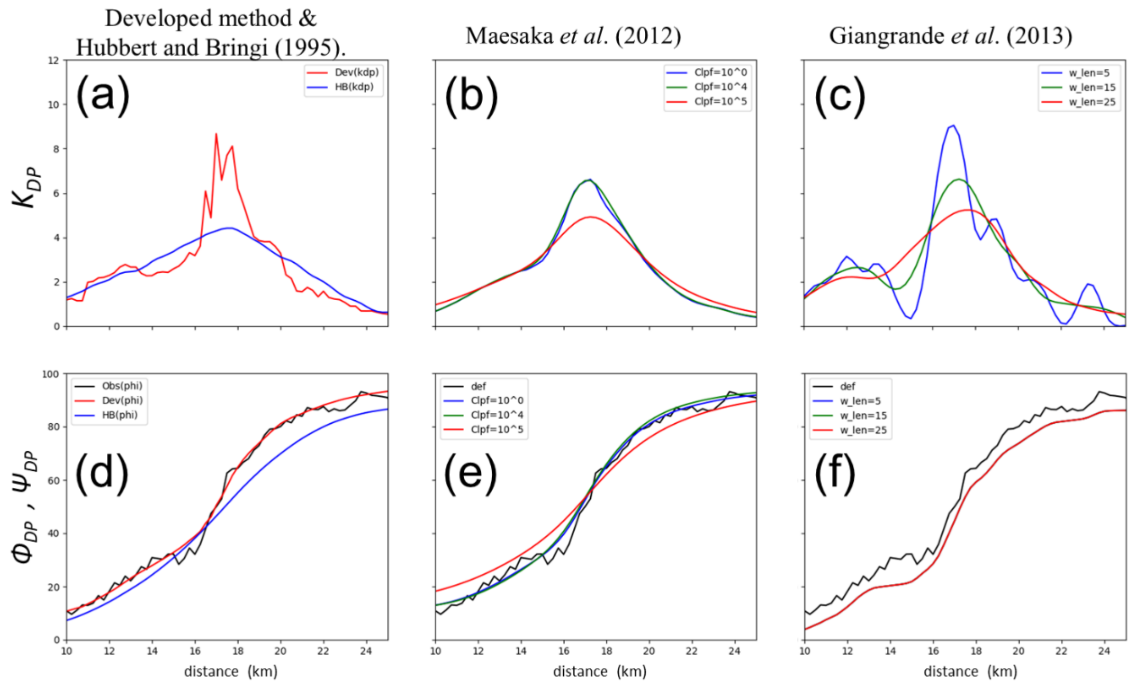

Figure 12: Distributions of K_{DP} (top panels) and Φ_{DP}, Ψ_{DP} (bottom panels) along the A–B line in Fig. 10 for each algorithm. (a) Blue: developed algorithm (K_{DP}); red: K_{DP} derived from Hubbert and Bringi (1995). (b) K_{DP} from Maesaka *et al.* (2012) with three parameter settings ($C_{lpf} = 10^0$, 10^{-4}, 10^{-5} shown in blue, green, and red, respectively). (c) K_{DP} from Giangrande *et al.* (2013) with three window lengths (w_len = 5, 20, 35) shown in blue, green, and red, respectively. (d–f) Corresponding Φ_{DP} with Ψ_{DP} (black). Note: Φ_{DP} in panel (d) was obtained by range integration of K_{DP}.

4.5 Validity of radial integration of K_{DP}

The proposed algorithm estimated K_{DP} at each grid point from Ψ_{DP} using scale-adaptive fitting, which did not guarantee the conservation of Φ_{DP}, a cumulative quantity along the radial direction. Consequently, the accuracy of Φ_{DP} relied on the precision of the individual K_{DP} estimates.

Figure 13 extends the domain shown in Fig. 9b. The region of intense rainfall was located west of the radar, while a moderately strong echo region (>40 dBZ) associated with the melting layer appeared in the distant north (Fig. 13a). The estimated K_{DP} field reflected these features (Fig. 13b). The range-integrated K_{DP} yielded Φ_{DP} values that increased radially. Some regions exhibited phase wrapping and reached negative values down to −150° (Fig. 13c). The observed Ψ_{DP} (Fig. 13d) closely resembled the estimated Φ_{DP}, both in the weak rainfall area to the east and the area of strong echoes to the west and north. The indication was that noise was effectively suppressed, and K_{DP} was estimated in a stable and reasonable manner even under conditions of weak rainfall and melting ice layers.

The validity of the estimated Φ_{DP} strongly depended on the smoothing scale of the coefficient a in Eq. (5). Figure 14 shows the mean error between the observed Φ_{DP} and Ψ_{DP} over the observation domain for each value of a. The smallest errors occurred near $a = 2$ (Fig. 14a). The indication was that higher-resolution settings (smaller a) resulted in insufficient suppression of noise and an overestimation of Φ_{DP}, whereas lower-resolution settings (larger a) led to an underestimation (negative bias) of Φ_{DP}. The RMSE also reached a minimum around $a = 2$ (Fig. 14b). However, these statistical patterns were dependent on the scale of the precipitation system. If the evaluation was intentionally focused on large-scale systems such as typhoons, high performance was maintained even with larger values of a that imposed stronger smoothing because the impact of smoothing was less pronounced in such cases (not shown).

However, localized issues remained. Non-uniform Partial Beam Filling (NPBF), for instance, introduces non-precipitation signals on scales larger than the noise assumed in the current algorithm. To achieve more robust, high-precision estimates of K_{DP}, further refinements based on a deep understanding of the algorithm's characteristics will be required.

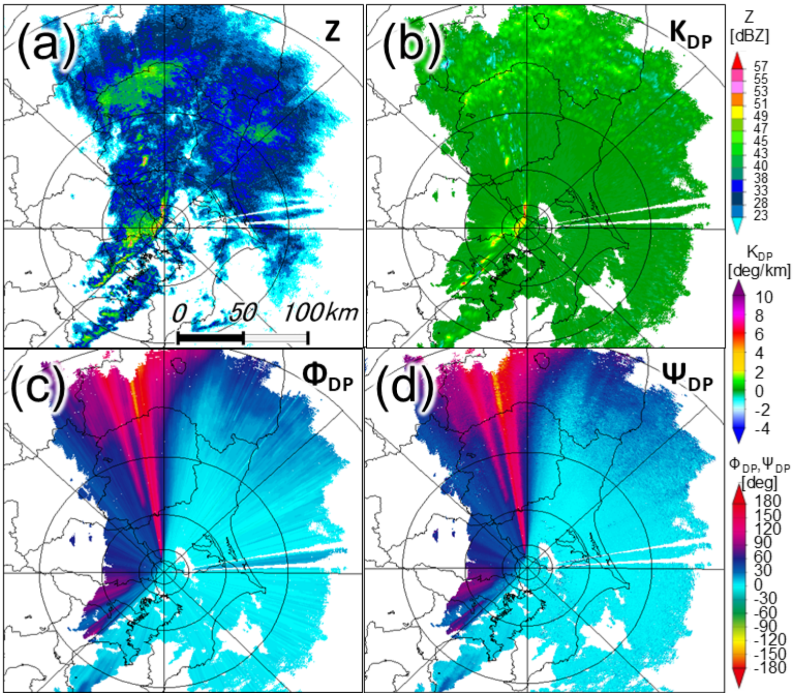

Figure 13: Wide-area distributions for the *Dev* case shown in Fig. 9b: (a) attenuation-corrected reflectivity Z; (b) specific differential phase K_{DP}; (c) differential phase Φ_{DP} estimated by range integration of K_{DP}; (d) observed differential phase Ψ_{DP}.

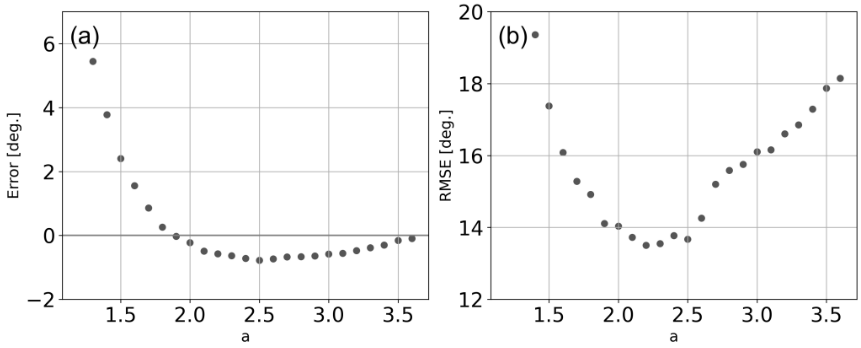

Figure 14: Statistical distributions of errors in Ψ_{DP} and Φ_{DP} for the Dev case in Fig. 9b, evaluated with varying the smoothing coefficient a: (a) mean error; (b) root mean square error (RMSE). Statistics are based on Plan Position Indicator data across elevation angles from 0.0° to 2.5°.

5 Summary

A K_{DP} estimation algorithm was developed using scale-adaptive fitting based on a local polynomial approximation. The Savitzky–Golay (SG) fitting enabled fast convolution-based processing. The regression window was dynamically adjusted to the characteristics of local data. In the proposed configuration, SG fitting is applied in two steps, and a noise-reduction mechanism is embedded between them to stably suppress random fluctuations of backscattering artifacts. The adaptive adjustment of the fitting window based on the estimated K_{DP} value enabled high spatial resolution for large K_{DP} and enhanced noise suppression for small K_{DP}. This design achieved both computational efficiency and estimation accuracy by balancing local resolution and smoothness.

Parameter settings were optimized using idealized experiments from previous studies, and the performance of the resulting configuration was evaluated by applying it to real radar data from cases of convective rainfall. Statistical analysis confirmed improved noise suppression in regions of weak rain and enhanced local resolution in areas of intense rain. Comparison with reflectivity fields showed that K_{DP} successfully reproduced the peak structures indicated by reflectivity. Comparison with other K_{DP} algorithms implemented in Py-ART revealed different resolution characteristics that depended on K_{DP} values; in particular, the developed method was associated with fine-scale fluctuations that avoided the oversmoothing typically inherent in regression-based estimations. Furthermore, the high consistency of the Φ_{DP} obtained by integration of the estimated K_{DP} using appropriate parameter settings with the observed Ψ_{DP} across the entire range indicated low overall error and strong agreement with actual measurements.

This study focused on balancing the noise–resolution trade-off within the framework of quasi-fixed window designs. Based on the development of a sequential computation method informed by this estimation, further refinement of local precision will be presented in a future paper alongside an expanded algorithm.

Appendix A: Treatment of negative K_{DP}

When the adaptive SG fitting uses a regression window defined as in Eq. (5), negative K_{DP} values may not be computed. To address this problem, a minimum threshold—analogous to the maximum expected in rainfall—is introduced to account for negative values. The window size in Eq. (A1) is then defined using $|K_{DP}|$ to enable both positive and negative values to be handled.

During sequential processing, sign reversal of K_{DP} may occur. To avoid instability caused by sign reversal, the algorithm retains the history of the window size *m* and previous K_{DP} values as defined in Eq. (6), and it incorporates the change into the window calculation in Eq. (A1).

$$\Delta\Phi_{DP} = \begin{cases} 2a\Delta r\left|K_{DP}^{max}\right|_{K_{DP}>0} \\ 2a\Delta r\left|K_{DP}^{min}\right|_{K_{DP}<0} \end{cases} . \tag{A1}$$

Appendix B: Extension of data range and data interpolation/extrapolation

For the processing of Ψ_{DP} to derive K_{DP}, uniformly spaced grid data are required for the local regression window. To meet this requirement, the computational data range is extended at both ends of the observation and at echo boundaries where data are missing. At echo edges, echo data are mirrored from the boundary to suppress noise amplification in regions of low signal-to-noise. For the same purpose, echo-free gaps are filled by interpolating the median values extracted from a selected number of surrounding echoes. To mitigate noise sensitivity, the computational range is adaptively adjusted to ensure a linear increase of values.

Near the radar centre, extrapolation is handled using one of several strategies depending on the situation: (i) setting Ψ_{DP} to zero, (ii) using the reversed value from the opposite azimuth (180°), or (iii) applying the mean azimuthal bias from surrounding echo regions. While outside the main scope of this study, there is room for further enhancement in these areas.

Appendix C: Pre-, internal, and post-computation quality control

The SG fitting, as a local regression-based operation, can be sensitive to numerical errors when the computational window is narrowed excessively. To ensure stability against observational noise under these conditions, a pre-processing quality control (QC) for Ψ_{DP} is implemented. Specifically, each grid value is compared with the respective medians calculated independently from ranges preceding and following the target grid. Values deviating and exhibiting non-precipitation behavior are replaced with the local average. This procedure is effective for suppressing low-elevation clutters. Furthermore, the two-step sequential computation enables additional suppression of outliers through inter-grid comparisons, incorporation of techniques such as interpolation from neighboring values, or replacement with values obtained in the previous computational step.

Appendix D: Computational efficiency

While a standard SG fitting with a fixed computational range offers extremely low computational costs, iterative convolution-based operations that dynamically adjust the window size introduce additional minor overhead. To mitigate this drawback, the algorithm identifies the areas requiring computation at the onset of SG to avoid unnecessary calculation where echoes are absent. Further, the fact that the algorithm stops the calculation if K_{DP} converges during the iterative process, regardless of the window size, also contributes to minor reductions in computational cost.

Data availability

The radar data provided by the Japan Meteorological Agency are not publicly available. Access requires permission from the JMA.

Author contributions

NN designed the methodology, conducted the investigation process, collected the data, and performed the formal analysis of the data and visualization; HY proposed the research goals and aims; NN prepared the paper draft; and NN and HY reviewed, commented on, and edited the paper.

Competing interests

The contact author has declared that none of the authors has any competing interests.

Acknowledgements

Several useful comments by two anonymous reviewers are gratefully acknowledged because they significantly improved the original manuscript. NN also thanks Dr. Takashi Unuma (Meteorological Research Institute; MRI) for his helpful guidance on the use of Py-ART.

References

Aldana, M., Pulkkinen, S., von Lerber, A., Kumjian, M. R., and Moisseev, D.: Benchmarking K_{DP} in rainfall: a quantitative assessment of estimation algorithms using C-band weather radar observations, Atmos. Meas. Tech., 18, 793–816, https://doi.org/10.5194/amt-18-793-2025, 2025.

Brandes, E. A., Zhang, G., and Vivekanandan, J.: Experiments in rainfall estimation with a polarimetric radar in a subtropical environment, J. Appl. Meteorol. Clim., 41, 674–685, https://doi.org/10.1175/1520-0450(2002)041<0674:EIREWA>2.0.CO;2, 2002.

Bringi, V. N. and Chandrasekar, V.: Polarimetric Doppler Weather Radar: Principles and Applications, Cambridge University Press, Cambridge, https://doi.org/10.1017/CBO9780511546075, 2001.

Giangrande, S. E., McGraw, R., and Lei, L.: An Application of Linear Programming to Polarimetric Radar Differential Phase Processing, J. Atmos. Ocean. Tech., 30, 1716–1729, https://doi.org/10.1175/JTECH-D-12-00147.1, 2013.

Gorgucci, E., Scarchilli, G., and Chandrasekar, V.: Specific differential phase estimation in the presence of nonuniform rainfall medium along the path, J. Atmos. Ocean. Tech., 16, 1690–1697, https://doi.org/10.1175/1520-0426(1999)016<1690:SDPEIT>2.0.CO;2, 1999.

Helmus, J. J. and Collis, S. M.: The Python ARM Radar Toolkit (Py-ART), a library for working with weather radar data in the Python programming language, J. Open Res. Softw., 4, e25, https://doi.org/10.5334/jors.119, 2016.

Hubbert, J. and Bringi, V. N.: An iterative filtering technique for the analysis of copolar differential phase and dual-frequency radar measurements, J. Atmos. Ocean. Tech., 12, 643–648, https://doi.org/10.1175/1520-0426(1995)012<0643:AIFTFT>2.0.CO;2, 1995.

Jameson, A. R.: The Effect of Temperature on Attenuation-Correction Schemes in Rain Using Polarization Propagation Differential Phase Shift, J. Appl. Meteorol., 31, 719–746, https://doi.org/10.1175/1520-0450(1992)031<0719:TEOTOA>2.0.CO;2, 1992.

Liu, L., Bringi, V. N., Chandrasekar, V., Mueller, E. A., and Mudukutore, A.: Analysis of the copolar correlation coefficient between horizontal and vertical polarizations, J. Atmos. Ocean. Tech., 11, 950–963, https://doi.org/10.1175/1520-0426(1994)011<0950:AOTCCC>2.0.CO;2, 1994.

Maesaka, T., Iwanami, K., and Maki, M.: Non-negative K_{DP} estimation by monotone increasing Φ_{DP} assumption below melting layer, 7th European Conf. on Radar in Meteorology and Hydrology (ERAD), Toulouse, France, 2012.

Marshall, J. S. and Palmer, W. M.: The distribution of raindrops with size, J. Meteorol., 5, 165–166, https://doi.org/10.1175/1520-0469(1948)005<0165:TDORWS>2.0.CO;2, 1948.Reimel, K. J. and Kumjian, M. R.: Evaluation of K_{DP} estimation algorithm performance in rain using a known-truth framework, J. Atmos. Ocean. Tech., 38, 587–605, https://doi.org/10.1175/JTECH-D-20-0060.1, 2021.

Romine, G. S., Burgess, D. W., and Wilhelmson, R. B.: A dual-polarization-radar-based assessment of the 8 May 2003 Oklahoma City area tornadic supercell, Mon. Weather Rev., 136, 2849–2870, https://doi.org/10.1175/2008MWR2330.1, 2008.

Ryzhkov, A. V. and Zrnić, D. S.: Comparison of dual-polarization radar estimators of rain, J. Atmos. Ocean. Tech., 12, 249–256, https://doi.org/10.1175/1520-0426(1995)012<0249:CODPRE>2.0.CO;2, 1995.

Ryzhkov, A. V. and Zrnić, D. S.: Radar Polarimetry for Weather Observations, Springer International Publishing, Cham, https://doi.org/10.1007/978-3-030-05093-1, 2019.

Ryzhkov, A., Kumjian, M., Ganson, S., and Khain, A.: Polarimetric Radar Characteristics of Melting Hail. Part I: Theoretical Simulations Using Spectral Microphysical Modeling, J. Appl. Meteorol. Clim., 52, 2849–2870, https://doi.org/10.1175/JAMC-D-13-073.1, 2013.

Savitzky, A. and Golay, M. J. E.: Smoothing and differentiation of data by simplified Least-Squares procedures, Anal. Chem., 36, 1627–1639, https://doi.org/10.1021/ac60214a047, 1964.

Schneebeli, M., Grazioli, J., and Berne, A.: Improved estimation of the specific differential phase shift using a compilation of Kalman filter ensembles, IEEE Trans. Geosci. Remote Sens., 52, 5137–5149, https://doi.org/10.1109/TGRS.2013.2287017, 2014.

Vulpiani, G., Montopoli, M., Passeri, L. D., Gioia, A. G., Giordano, P., and Marzano, F. S.: On the Use of Dual-Polarized C-Band Radar for Operational Rainfall Retrieval in Mountainous Areas, J. Appl. Meteorol. Clim., 51, 405–425, https://doi.org/10.1175/JAMC-D-10-05024.1, 2012.

Wang, Y. and Chandrasekar, V.: Algorithm for estimation of the specific differential phase, J. Atmos. Ocean. Tech., 26, 2569–2582, https://doi.org/10.1175/2009JTECHA1358.1, 2009.

Wilson, M. B. and Van Den Broeke, M. S.: An automated Python algorithm to quantify Z_{DR} arc and K_{DP}–Z_{DR} separation signatures in supercells, J. Atmos. Ocean. Tech., 38, 371–386, https://doi.org/10.1175/JTECH-D-20-0056.1, 2021.